

Precise, super-resolving intensity measurement by quantum jump spectroscopy of a single neutral atom

Lorena C. Bianchet,¹ Natalia Alves,¹ Laura Zarraoa,¹ Tomas Lamich,¹ Vindhiya Prakash,¹ and Morgan W. Mitchell^{1,2}

¹*ICFO - Institut de Ciències Fotoniques, The Barcelona Institute of Science and Technology, 08860 Castelldefels, Barcelona, Spain*

²*ICREA - Institució Catalana de Recerca i Estudis Avançats, 08010 Barcelona, Spain*

We employ a single trapped ^{87}Rb atom as a sub-wavelength optical intensity sensor, by spectroscopic measurement of the ac Stark shifts on the $F = 1 \rightarrow F' = 2$ hyperfine transition of the D_2 line. This transition experiences very small tensor light shifts, allowing a precise measurement of the scalar shift caused by a linearly-polarized field. A “quantum jump” technique, in which a single photon absorbed on the transition of interest induces the scattering of hundreds of photons on a bright, closed transition, is used to boost signal level and avoid systematic effects such as probe-induced optical pumping. The resulting line shape is used to extract the intensity at trap focus and the atom temperature. The analogous probing method on the $F = 1 \rightarrow F' = 1$ transition, in contrast, experiences strong tensor light shifts, and may be useful in Zeeman-state-resolving detection.

Individual trapped ions and neutral atoms can be positioned with sub-micrometer precision, and have been used to detect a variety of environmental perturbations, including static [1] and oscillating [2] magnetic fields, static electric fields [3], and microwaves [4]. Measurement of optical intensity, which in many scenarios varies on micrometer scales, is a natural application for such sensors [5, 6]. Sub-wavelength (a.k.a. super-resolving) measurement of both resonant [5] and off-resonant light [6, 7] have been demonstrated. Single atoms and ions are also ideal for metrology referenced to unchanging atomic properties, e.g., polarizabilities that can be calculated with high precision [8, 9]. Single trapped atoms thus offer a route to precision radiometry with high spatial resolution.

Off-resonance light, which for any given atom constitutes the vast majority of the optical spectrum, can be detected by the ac Stark shifts it produces on observable spectral lines. For example, single neutral ^{87}Rb atoms in far-off-resonance traps (FORTs) have been used to quantify ac Stark shifts by monitoring fluorescence on the $F = 2 \rightarrow F' = 3$ cooling transition of the D_2 line [6, 7, 10]. While this strong, closed transition is convenient, it is not naturally suited for precision measurement because it, like other strong closed transitions, has large vector and tensor polarizabilities. This implies 1) that a scalar ac Stark shift to be detected will necessarily be accompanied by a broadening or splitting of the resonance fluorescence line [7] and 2) that the resonance fluorescence intensity will depend on the polarization of the excitation light, the atomic Zeeman state, and, via the FORT intensity distribution, also the atomic position. These atomic attributes are easily perturbed by the resonance fluorescence process itself, which modifies the atom’s internal state through optical pumping, and its position through recoil effects [7]. All these factors complicate the interpretation of the acquired spectra.

Here, we introduce a single-atom probing method that greatly reduces these systematic effects, through the use of an open transition and “quantum jump” readout [11–

15] to amplify the resulting signal at very low probe power levels. We apply the technique to measure the intensity distribution seen by an atom in an optical tweezer, i.e., a strongly-focused FORT [16], of the sort used to study quantum light-matter interactions [17–22], non-classical atom interference effects [10, 23–25], Rydberg-atom-based quantum information processing [26] and quantum simulation [27, 28]. In this application, the method reveals both the trap-center intensity with high precision, and also the atom temperature, both of which are subject to considerable systematic uncertainty when measured by other methods [29].

The method, illustrated in Figure 1, is a spectroscopic probe of the open $1 \rightarrow 2'$ transition of the D_2 line, i.e. $5\text{S}_{1/2}F = 1 \rightarrow 5\text{P}_{3/2}F' = 2$ (for brevity, we indicate the ground and excited hyperfine states of this transition with unprimed and primed symbols) that, rather than detecting fluorescence on this transition, detects the induced state change using quantum jump physics, previously studied with ions [11, 12], molecules [13], cavity-bound photons [14] and quantum dots [15]. A weak probe beam, tuned near the $1 \rightarrow 2'$ transition, can promote the atom to the $F = 2$ “bright” ground state by a resonant Raman transition. From there, counter-propagating cooler beams drive resonance fluorescence on the closed $2 \rightarrow 3'$ transition, Rayleigh scattering hundreds of photons on average before the atom spontaneously falls back to the $F = 1$ “dark” ground state. The probe and cooler beams are on continuously, so the atom stochastically emits bursts of resonance fluorescence at an average rate set by the rate of $1 \rightarrow 2'$ excitation. The probe detuning is scanned across the $1 \rightarrow 2'$ line to reveal the ac Stark shifted spectrum of that transition. We refer to this method as *quantum jump spectroscopy*.

In this method, resonance fluorescence acts as a high-gain amplifier, scattering many cooler photons for each $1 \rightarrow 2' \rightarrow 2$ Raman transition. The amplification gain depends on properties of the cooler light, magnetic fields, trap geometry, and detection efficiencies, all of which can

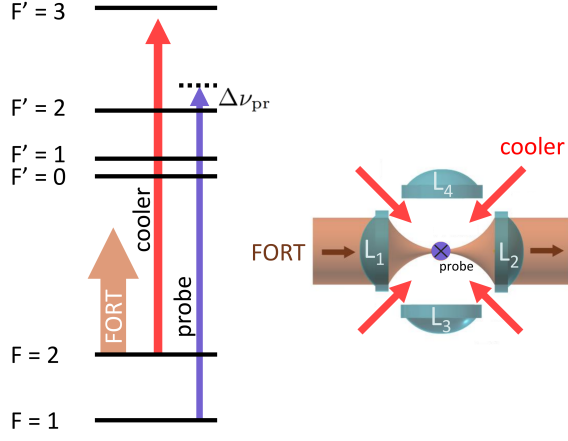


FIG. 1. Principle of the quantum jump spectroscopy method. (Left) Relevant levels of ^{87}Rb $5S_{1/2} \rightarrow 5P_{3/2}$, D_2 transition. Resonance fluorescence is produced on the closed $2 \rightarrow 3'$ hyperfine transition from the $F = 2$ “bright” state, whereas the $F = 1$ “dark” state does not fluoresce. A probe beam with a frequency detuning of $\Delta\nu_{\text{pr}}$ from the $1 \rightarrow 2'$ transition can cause Raman transitions to the bright state, resulting in a “quantum jump” - a burst of resonance fluorescence that greatly amplifies the effect of the single-photon scattering event that caused the jump. The resonance fluorescence also cools the atom’s center of mass motion, returning it to a probe-independent state before the next probe absorption. (Right) Geometry of the experiment, viewed from above. Four in-vacuum high numerical-aperture lenses (L1 to L4) collect resonance fluorescence, and also serve to produce the strongly focused FORT. Re-pumper propagates together with the four horizontal cooler beams. Circularly-polarized probe beam propagates in the vertical direction (perpendicular to the plane of the figure), together with the fifth and sixth cooler beams (not shown).

be held constant as the probe frequency is scanned. In addition, the resonance fluorescence process returns the atom to the $F = 1$ state with an internal- and center-of-mass state determined by the resonance fluorescence process, erasing any probe-induced heating or optical pumping. Finally, the $1 \rightarrow 2'$ transition has a very small tensor susceptibility. Together, these features greatly simplify the interpretation of spectra, relative to earlier methods [6, 7, 10].

To demonstrate intensity measurement by quantum jump spectroscopy, we employ a Maltese cross single atom trap [29, 30], in which a magneto-optical trap (MOT) with cooler light red-detuned by $4\gamma_0 = 2\pi \times 36$ MHz from the unshifted $2 \rightarrow 3'$ transition is used to load the FORT, and also provides cooler light for the quantum jump spectroscopy. The MOT re-pumper is stabilized near the $1 \rightarrow 1'$ transition.

The FORT light is linearly polarized and stabilized to the Cs D_2 line at 852.1 nm, with an input power of $P_{\text{FORT}} = 6.8(2)$ mW, measured with a power meter be-

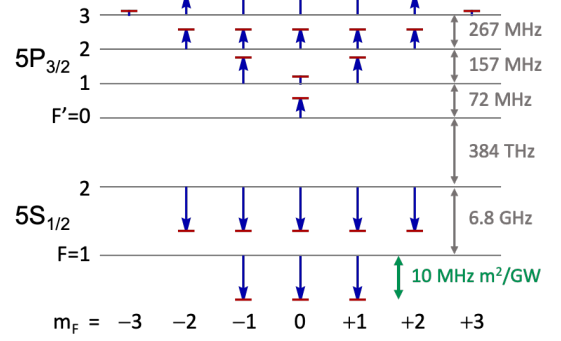


FIG. 2. Level shifts for the D_2 line of ^{87}Rb under linearly-polarized illumination at 852 nm, computed as in [9]. Red lines above/below blue arrows show shifted Zeeman sublevels corresponding to the m_F labels below. Blue arrows show the ac Stark shifts per intensity (scale in green at lower right), relative to the unshifted hyperfine levels (grey horizontal lines). Hyperfine level spacings not to scale.

fore the chamber window. The FORT has an intensity at focus, estimated from the input power and beam waist prior to focusing, of $I_{\text{FORT}}^{(\text{max})} \approx 1.6 \times 10^9 \text{ W m}^{-2}$ [29]. As shown in Figure 2, this implies a light shift of ≈ 20 MHz on the $1 \rightarrow F'$ transitions. We note that the $1 \rightarrow 2'$ transition experiences negligible tensor light shifts, with the consequence that the resonance frequency depends on the atom’s position, but not the atom’s internal state.

A circularly-polarized probe beam with up to 800 nW of power in a collimated beam with 2 mm $1/e^2$ diameter and tunable over 30 MHz on the blue side of the unshifted $1 \rightarrow 2'$ transition with a double-pass AOM, is sent along the downward vertical direction, co-propagating with one of the MOT cooler beams. Fluorescence is collected by three high-NA lenses (L1, L2 and L4) surrounding the trap center, coupled into single-mode fibers, registered with avalanche photodiodes (APDs) and counted in 20 ms time bins.

To acquire fluorescence signals versus probe intensity and versus detuning, we implemented the sequence shown in Figure 3 (upper): starting from an empty FORT, the MOT beams (cooler and re-pumper) are turned on to allow an atom to be trapped. Prior to the atom’s arrival, the background count rate is recorded. Arrival of an atom is determined when the detected count in channel L1 is above 50 photons per bin. After this “trigger” event, re-pumper and cooler remain on for 60 ms to cool the trapped atom. The re-pumper is then turned off for 300 ms, leaving cooler and probe on, to record probe-and-cooler induced fluorescence. The re-pumper is then turned on again for 60 ms, to check if the atom is still trapped. The cooler and re-pumper are then turned off. The atom is allowed to leave by turning off the FORT and cooling beams, and the cycle repeats.

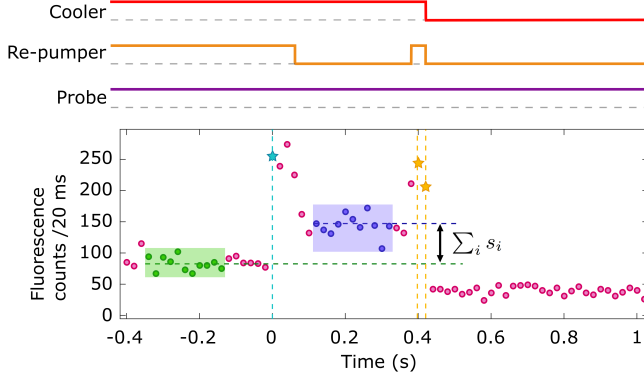


FIG. 3. Sequence and representative fluorescence signal from a single atom. Upper portion shows time sequence of the cooler, re-pumper and probe light. Dashed lines indicate the respective zero levels. Lower portion shows observed fluorescence counts in 20 ms bins, obtained by pooling counts from the L1, L2 and L4 channels. First detection of an atom in the trap (cyan star) triggers the rest of the sequence, and is taken as the time origin (cyan line). Purple points $d_{i,t}$ are used to calculate s_i the rate of atom fluorescence collected by channel i , green points $b_{i,t}$ are used to calculate background due to laser scattering and counts marked with yellow stars (and yellow lines) are used to verify atom survival.

The probe is on at constant power and frequency during this whole sequence.

As illustrated in Figure 3 (lower), we record detections $d_{i,t}$ (shown in purple) and background counts $b_{i,t}$ (shown in green) from each trapped atom for a total time of 220 ms divided in 11 time bins, where i indicates the APD channel (and thus also the lens) in which the photons are collected and $t \in \{1, \dots, 11\}$ labels the time bin. For any given probe detuning and power, we measure 20 trials like the one shown in Figure 3. About 65 % of the atoms survive. We pool the resulting $d_{i,t}$ and $b_{i,t}$ values, to have $N \approx 200$ values of each kind.

To extract a signal value and error from these data, we assume $b_{i,t}$ and $d_{i,t}$ have means c_i and $c_i + s_i$, respectively, and variances $\sigma_{i,b}^2$ and $\sigma_{i,d}^2$ respectively. That is, c_i is the mean background rate, while s_i is the mean atom scattering collected by each channel. Different t values are assumed independent. s_i is estimated as the sample mean of $\{d_{i,t} - b_{i,t}\}$. We estimate $\sigma_{i,d}^2$ and $\sigma_{i,b}^2$ as the sample variances of $\{d_{i,t}\}$ and $\{b_{i,t}\}$, from which we estimate $\sigma_{s_i}^2 = \sigma_{i,d}^2 + \sigma_{i,b}^2$. Error estimates are propagated from these variances. The atom scattering is also defined as $s_i \equiv \zeta_i S$ with ζ_i is the channel quantum efficiency, comprising collection, transmission, and detection efficiencies and S is the rate of photon scattering by the atom.

Representative fluorescence signals as a function of probe intensity I_{pr} and detuning $\Delta\nu_{\text{pr}}$ are shown in Figure 4. We note that, with ≈ 13 atoms per point (requiring less than 6 s of measurement), the technique resolves detunings in steps of $\gamma_0/2$, where γ_0 is the natural linewidth

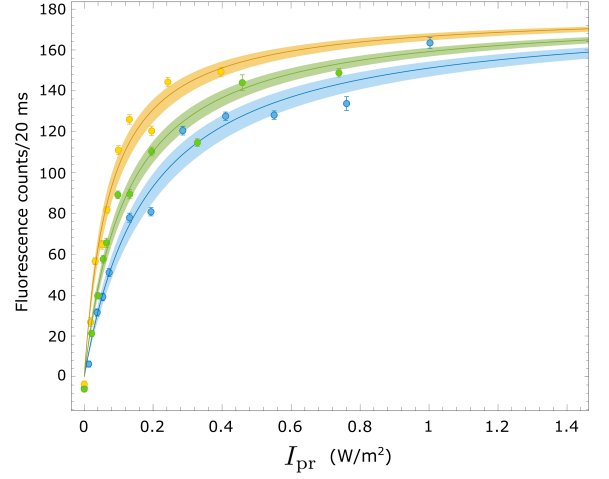


FIG. 4. Collected resonance fluorescence rates as a function of probe intensity I_{pr} and detuning $\Delta\nu_{\text{pr}}$. Vertical axis shows the net collected signal $\sum_i s_i$ with $i \in \{L_1, L_2, L_4\}$, where $s_i = \langle d_{i,t} - b_{i,t} \rangle$ is averaged over 11 time bins per atom, acquired in 220 ms (20 ms per time bin), and over 11 to 19 atoms. Upper (orange), middle (green) and lower (blue) curves show detunings $\Delta\nu_{\text{pr}} = \gamma_0/2$, γ_0 and $3\gamma_0/2$, respectively, from the frequency $\nu_{1 \rightarrow 2'}$ of the unshifted $1 \rightarrow 2'$ transition. Error bars show plus/minus one standard error of the mean. Curves show fits with $\sum_i s_i = \sum_i s_i^{(\text{max})} I_{\text{pr}} / (I_{\text{pr}} + I_{\text{sat}})$, with $\sum_i s_i^{(\text{max})} = 179$ counts/20 ms (found by averaging best-fit values for $\sum_i s_i^{(\text{max})}$ of the individual detunings) and best-fit values $1/I_{\text{sat}} = \eta(\nu_{1 \rightarrow 2'} + \Delta\nu_{\text{pr}})/\Gamma = 13.6(22) \text{ m}^2 \text{ W}^{-1}$, $8.1(10) \text{ m}^2 \text{ W}^{-1}$ and $5.4(9) \text{ m}^2 \text{ W}^{-1}$ for $\Delta\nu_{\text{pr}} = \gamma_0/2$, γ_0 and $3\gamma_0/2$, respectively. Color shadow considers fitting errors.

of the D_2 transition, and also probe intensity differences of order 10 mW m^{-2} , four orders of magnitude below the 16.69 W m^{-2} saturation intensity of the D_2 line [31].

The observed saturation behavior is well explained with a steady-state rate equation model: the rate of $1 \rightarrow 2$ transitions is $I_{\text{pr}} \eta(\nu_{\text{pr}}) P_1$, where $P_1 = 1 - P_2$ is the probability to be in the $F = 1$ ground state whereas P_2 is the probability to be in the $F = 2$ ground state, I_{pr} is the probe intensity at the atom, $\nu_{\text{pr}} \equiv \nu_{1 \rightarrow 2'} + \Delta\nu_{\text{pr}}$ is the probe's line-center linear frequency, where $\nu_{1 \rightarrow 2'}$ is the frequency of the unshifted $1 \rightarrow 2'$ transition, and $\eta(\nu_{\text{pr}})$ is the efficiency of $1 \rightarrow 2'$ excitation, i.e., the spectral function we seek to measure. The rate of $2 \rightarrow 1$ transitions is ΓP_2 , where Γ is a return rate that depends on the characteristics of the cooler and the $2 \rightarrow F'$ transitions, but is independent of the probe. The steady-state condition is $P_2 = x/(1 + x)$, where the saturation parameter x is defined as

$$x(\nu_{\text{pr}}) \equiv I_{\text{pr}} \eta(\nu_{\text{pr}}) / \Gamma. \quad (1)$$

Finally, we assume the atom emits fluorescence at a rate $S = S_{\text{max}} P_2$, such that

$$S = S_{\text{max}} \frac{I_{\text{pr}}}{I_{\text{pr}} + I_{\text{sat}}} \quad (2)$$

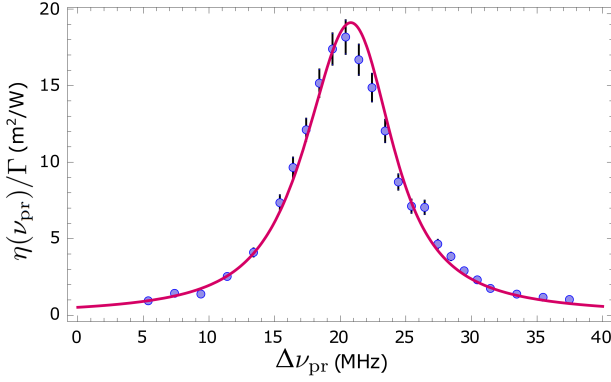


FIG. 5. Quantum jump spectroscopy of the $5S_{1/2}, F = 1 \rightarrow 5P_{3/2}, F' = 2$ transition in individual FORT-trapped atoms. Horizontal axis shows detuning $\Delta\nu_{\text{pr}}$ from the unshifted $\nu_{1 \rightarrow 2'}$ transition frequency. Vertical axis shows excitation efficiency $\eta(\nu_{\text{pr}})/\Gamma$ computed via Equation 1. Sequences in which the atom escapes the trap are excluded in post-selection. Each point represents the average of 30 atoms. Error bars indicate plus/minus one standard error. Background counts, measured with no atom in the trap, have been subtracted. Curves show a fit with Equation 4, with FORT intensity at trap center and atom temperature as free parameters. The fit finds $I_{\text{FORT}}^{(\text{max})} = 1.593(5) \times 10^9 \text{ W m}^{-2}$ at trap center and $T = 36.7(8) \text{ } \mu\text{K}$, with r.m.s. statistical uncertainties found by bootstrapping. These values are in good agreement with independent measurements.

where $I_{\text{sat}} = \Gamma/\eta(\nu_{\text{pr}})$ is the saturation intensity for the fluorescence process as a whole. As described in the caption of Figure 4, we fit fluorescence data versus power to obtain values for $s_i^{(\text{max})} = \zeta_i S_{\text{max}}$.

To measure spectra, we set the probe frequency ν_{pr} , adjust I_{pr} by eye to achieve $S/S_{\text{max}} \approx 1/3$ (and thus $x \approx 1/2$), and record the resulting I_{pr} value with a power meter before the vacuum chamber window. We then acquire traces like the ones shown in Figure 3. Using $s_i^{(\text{max})}$ from the prior calibration, s_i and $\sigma_{s_i}^2$ estimated from the observed $\{d_{i,t}\}$ and $\{b_{i,t}\}$, we compute $x_i \equiv s_i/(s_i^{(\text{max})} - s_i)$, $i \in \{L_1, L_2, L_4\}$ with corresponding variances $\sigma_{x_i}^2$, and estimate x as their weighted average. Finally, we find $\eta(\nu_{\text{pr}})/\Gamma = x/I_{\text{pr}}$ using Equation 1. A representative spectrum is shown in Figure 5.

Via light shifts, this spectrum gives information on both the FORT intensity and thus beam shape, and on the atomic center-of-mass spatial distribution and thus atom temperature. If the probe laser instantaneous frequency is ν , and the instantaneous light-shift is $\Delta_{eg} = (\delta_e - \delta_g)I_{\text{FORT}}(\mathbf{x})$, where δ_e, δ_g are the per-intensity light shifts of the excited and ground state, respectively, and \mathbf{x} is the instantaneous position of the atom, then the instantaneous efficiency of excitation is

$$\eta \propto f_{\text{nat}}(\nu_{eg} + \Delta_{eg} - \nu), \quad (3)$$

where $\nu_{eg} = (E_e - E_g)/2\pi\hbar$ is the unshifted line center

and $f_{\text{nat}}(\nu) \propto 1/[(\gamma_0/2)^2 + (2\pi\nu)^2]$ is the natural line shape function. Averaging over the distribution of light shifts $f_{\Delta}(\Delta_{eg})$, and the probe laser's line-shape function $f_{\text{pr}}(\delta)$, with $\delta \equiv \nu - \nu_{\text{pr}}$, we obtain

$$\eta(\nu_{\text{pr}}) \propto \int d\delta d\Delta_{eg} f_{\text{nat}}(\nu_{eg} + \Delta_{eg} - \nu_{\text{pr}} - \delta) \times f_{\text{pr}}(\delta) f_{\Delta}(\Delta_{eg}), \quad (4)$$

i.e., the convolution of $f_{\text{nat}}(\nu)$ with $f_{\text{pr}}(\delta)$ and $f_{\Delta}(-\Delta_{eg})$.

To relate this to the atom temperature, we note that the optical potential is $V = \alpha\Delta_{eg}$, where $\alpha \equiv 2\pi\hbar\delta_g/(\delta_e - \delta_g)$. Assuming the atom's center-of-mass coordinate is thermally distributed, f_{Δ} is given by a Boltzmann distribution $f_{\Delta} \propto \exp[-\beta V]\rho(V)$, where $\beta \equiv 1/k_B T$ and $\rho(V)$ is the potential density of states. If the potential is quadratic with minimum V_{min} , this gives

$$f_{\Delta}(\Delta) \propto \sqrt{\alpha\Delta - V_{\text{min}}} e^{-\beta(\alpha\Delta - V_{\text{min}})} \beta^{3/2} \quad (5)$$

for $\alpha\Delta > V_{\text{min}}$, and zero otherwise.

The line center reflects the average light shift, which depends strongly on the maximum intensity $I_{\text{FORT}}^{(\text{max})} \equiv \max_{\mathbf{x}} I_{\text{FORT}}(\mathbf{x})$ and weakly on the temperature T , whereas the line width depends more strongly on T . Fitting the data of Figure 5, and using a bootstrapping procedure to estimate the fitting uncertainties, we find $I_{\text{FORT}}^{(\text{max})} = 1.593(5) \times 10^9 \text{ W m}^{-2}$ and a temperature $T = 36.7(8) \text{ } \mu\text{K}$. The reduced χ^2 of this fit is 3.8, which suggests that there are other perturbations roughly comparable to these statistical uncertainties. Relating the obtained value of $I_{\text{FORT}}^{(\text{max})}$ with the waist w of the FORT beam, defined as the $1/e^2$ radius of intensity, and assuming the Gaussian beam relation $I_{\text{FORT}}^{(\text{max})} = 2P_{\text{FORT}}/\pi w^2$ with $P_{\text{FORT}} = 6.8(2) \text{ mW}$ the power of the beam used for the FORT, the waist is $w = 1.65(2) \text{ } \mu\text{m}$, in good agreement with prior estimates [29]. The implied r.m.s. width of the center-of-mass distribution is $0.184 \text{ } \mu\text{m}$ in the radial directions and $1.58 \text{ } \mu\text{m}$ in the longitudinal, so the atom samples the FORT intensity distribution with sub-wavelength transverse resolution.

We note a possible extension of the technique: the spectroscopy could be performed with the probe tuned to the $1 \rightarrow 1'$ transition. On this transition, the excitation efficiency will be strongly Zeeman-state and probe-polarization dependent, due to selection rules and strong tensor light shifts of the $F' = 1$ state, as shown in Figure 2. These features enable internal-state-selective detection with the same advantages of high gain and low perturbation that we have demonstrated using the $1 \rightarrow 2'$ transition.

Conclusion – We have proposed and demonstrated the use a single neutral ^{87}Rb atom for precision, sub-wavelength sensing of optical intensity, implemented by a quantum jump spectroscopy technique. A very low intensity probe near the $F = 1 \rightarrow F' = 2$ hyperfine transition of the D_2 line drives “quantum jumps,” i.e.,

resonant Raman transitions, into the $F = 2$ ground state. A second laser near the $F = 2 \rightarrow F' = 3$ cycling transition induces a burst of resonance fluorescence for each Raman transition, greatly amplifying the detectable signal. By scanning the probe frequency, the spectrum of $F = 1 \rightarrow F' = 2$ excitation is measured, indicating the distribution of ac Stark shifts on this transition, which suffers negligible broadening from tensor light shifts. From this spectrum we obtain the intensity at trap centre and the atom's temperature. The technique can be extended to perform Zeeman-state-selective readout.

This work was supported by H2020 Future and Emerging Technologies Quantum Technologies Flagship projects macQsimal (Grant Agreement No. 820393) and QRANGE (Grant Agreement No. 820405); Marie Skłodowska-Curie grant agreement No. 847517, Spanish Ministry of Science projects OCARINA (Grant No. PGC2018-097056-B-I00), 17FUN03 USOQS, which has received funding from the EMPIR programme co-financed by the Participating States and from the European Union's Horizon 2020 research and innovation programme; “La Caixa” Foundation under agreement (LCF/BQ/SO15/52260044); and “Severo Ochoa” Center of Excellence CEX2019-000910-S Generalitat de Catalunya through the CERCA program; Agència de Gestió d'Ajuts Universitaris i de Recerca Grant No. 2017-SGR-1354; Grant PRE2020-094392 financed by MCIN/AEI/10.13039/501100011033 and FSE “El FSE invierte en tu futuro”; Secretaria d'Universitats i Recerca del Departament d'Empresa i Coneixement de la Generalitat de Catalunya, co-funded by the European Union Regional Development Fund within the ERDF Operational Program of Catalunya (project QuantumCat, ref. 001-P-001644); Fundació Privada Cellex; Fundació Mir-Puig.

-
- [1] T. Ruster, H. Kaufmann, M. A. Luda, V. Kaushal, C. T. Schmiegelow, F. Schmidt-Kaler, and U. G. Poschinger, *Phys. Rev. X* **7**, 031050 (2017).
 - [2] S. Kotler, N. Akerman, Y. Glickman, A. Keselman, and R. Ozeri, *Nature* **473**, 61 (2011).
 - [3] M. J. Biercuk, H. Uys, J. W. Britton, A. P. VanDevender, and J. J. Bollinger, *Nature Nanotechnology* **5**, 646 (2010).
 - [4] M. Wahnschaffe, H. Hahn, G. Zarantonello, T. Dubielzig, S. Grondkowski, A. Bautista-Salvador, M. Kohnen, and C. Ospelkaus, *Applied Physics Letters* **110**, 034103 (2017).
 - [5] G. R. Guthöhrlein, M. Keller, K. Hayasaka, W. Lange, and H. Walther, *Nature* **414**, 49 (2001).
 - [6] E. Deist, J. A. Gerber, Y.-H. Lu, J. Zeiher, and D. M. Stamper-Kurn, *Phys. Rev. Lett.* **128**, 083201 (2022).
 - [7] C.-Y. Shih and M. S. Chapman, *Phys. Rev. A* **87**, 063408 (2013).
 - [8] M. S. Safronova, C. J. Williams, and C. W. Clark, *Phys. Rev. A* **69**, 022509 (2004).
 - [9] S. Coop, S. Palacios, P. Gomez, Y. N. M. de Escobar, T. Vanderbruggen, and M. W. Mitchell, *Opt. Express* **25**, 32550 (2017).
 - [10] A. M. Kaufman, B. J. Lester, C. M. Reynolds, M. L. Wall, M. Foss-Feig, K. R. A. Hazzard, A. M. Rey, and C. A. Regal, *Science* **345**, 306 (2014).
 - [11] P. O. Schmidt, T. Rosenband, C. Langer, W. M. Itano, J. C. Bergquist, and D. J. Wineland, *Science* **309**, 749 (2005).
 - [12] A. H. Myerson, D. J. Szwer, S. C. Webster, D. T. C. Allcock, M. J. Curtis, G. Imreh, J. A. Sherman, D. N. Stacey, A. M. Steane, and D. M. Lucas, *Phys. Rev. Lett.* **100**, 200502 (2008).
 - [13] T. Basché, S. Kummer, and C. Bräuchle, *Nature* **373**, 132 (1995).
 - [14] S. Gleyzes, S. Kuhr, C. Guerlin, J. Bernu, S. Deléglise, U. Busk Hoff, M. Brune, J.-M. Raimond, and S. Haroche, *Nature* **446**, 297 (2007).
 - [15] A. N. Vamivakas, C. Y. Lu, C. Matthiesen, Y. Zhao, S. Fält, A. Badolato, and M. Atatüre, *Nature* **467**, 297 (2010).
 - [16] N. Schlosser, G. Reymond, I. Protsenko, and P. Grangier, *Nature* **411**, 1024 (2001).
 - [17] Y.-S. Chin, M. Steiner, and C. Kurtsiefer, *Nature Communications* **8**, 1200 (2017).
 - [18] S. A. Aljunid, M. K. Tey, B. Chng, T. Liew, G. Maslennikov, V. Scarani, and C. Kurtsiefer, *Phys. Rev. Lett.* **103**, 153601 (2009).
 - [19] V. Leong, M. A. Seidler, M. Steiner, A. Cerè, and C. Kurtsiefer, *Nature Communications* **7**, 13716 (2016).
 - [20] A. Asenjo-Garcia, M. Moreno-Cardoner, A. Albrecht, H. J. Kimble, and D. E. Chang, *Phys. Rev. X* **7**, 031024 (2017).
 - [21] J. Perczel, J. Borregaard, D. E. Chang, H. Pichler, S. F. Yelin, P. Zoller, and M. D. Lukin, *Phys. Rev. Lett.* **119**, 023603 (2017).
 - [22] A. Albrecht, L. Henriët, A. Asenjo-Garcia, P. B. Dieterle, O. Painter, and D. E. Chang, *ArXiv e-prints* (2018), arXiv:1803.02115 [quant-ph].
 - [23] B. J. Lester, Y. Lin, M. O. Brown, A. M. Kaufman, R. J. Ball, E. Knill, A. M. Rey, and C. A. Regal, *Phys. Rev. Lett.* **120**, 193602 (2018).
 - [24] A. M. Kaufman, B. J. Lester, M. Foss-Feig, M. L. Wall, A. M. Rey, and C. A. Regal, *Nature* **527**, 208 (2015).
 - [25] A. Glicenstein, G. Ferioli, N. Šibalić, L. Brossard, I. Ferrier-Barbut, and A. Browaeys, *Phys. Rev. Lett.* **124**, 253602 (2020).
 - [26] M. Saffman, T. G. Walker, and K. Mølmer, *Rev. Mod. Phys.* **82**, 2313 (2010).
 - [27] H. Bernien, S. Schwartz, A. Keesling, H. Levine, A. Omran, H. Pichler, S. Choi, A. S. Zibrov, M. Endres, M. Greiner, V. Vuletić, and M. D. Lukin, *Nature* **551**, 579 (2017).
 - [28] H. Labuhn, D. Barredo, S. Ravets, S. de Léséleuc, T. Macrì, T. Lahaye, and A. Browaeys, *Nature* **534**, 667 (2016).
 - [29] L. Bianchet, N. Alves, L. Zarracoa, N. Bruno, and M. Mitchell, *Open Research Europe* **1** (2021).
 - [30] N. Bruno, L. C. Bianchet, V. Prakash, N. Li, N. Alves, and M. W. Mitchell, *Opt. Express* **27**, 31042 (2019).
 - [31] D. A. Steck, “Rubidium 87 D line data, revision 2.1.4,” Available online at <http://steck.us/alkalidata> (23 December 2010).